Soft Matter

PAPER

View Article Online
View Journal | View Issue

Cite this: *Soft Matter*, 2019, **15**, 973

Anomalous transport of magnetic colloids in a liquid crystal–magnetic colloid mixture

Gaurav P. Shrivastav * and Sabine H. L. Klapp*

Received 12th October 2018,
Accepted 2nd January 2019

DOI: 10.1039/c8sm02090f

rsc.li/soft-matter-journal

We report an extensive molecular dynamics study on the translational dynamics of a hybrid system composed of dipolar soft spheres (DSS), representing ferromagnetic particles, suspended in a liquid crystal (LC) matrix. We observe that the LC matrix strongly modifies the dynamics of the DSS. In the isotropic regime, the DSS show a crossover from subdiffusive to normal diffusive behavior at long times, with an increase of the subdiffusive regime as the dipolar coupling strength is increased. In the nematic regime, the LC matrix, due to the collective reorientation of LC particles, imposes a cylindrical confinement on the DSS chains. This leads to a diffusive dynamics of DSS along the nematic director and a subdiffusive dynamics (with an exponent of $\sim$0.5) in the perpendicular direction. The confinement provided by the LC matrix is also reflected by the oscillatory behavior of the components of the velocity autocorrelation function of the DSS in the nematic phase.

1 Introduction

Inclusions of nano-to-micro sized particles inside a liquid crystal (LC) matrix have offered a new paradigm for hybrid material design and applications of LCs beyond display materials.[1–3] This is one of the most propitious advances in materials science as the self-organizing tendency of LCs provides numerous possibilities of synthesizing fascinating bulk structured materials.[4] In this context, suspensions of magnetic particles inside a LC matrix have attracted particular attention in the past few decades. These systems, first introduced theoretically in a celebrated work by Brochard and de Gennes,[5] show a rich variety of self-assembled structures and have a wide range of biomedical and technical applications.[6–8] The first experimental realization of such suspensions was achieved by doping magnetic particles in a thermotropic LC host.[9] A further early experimental study was performed by Lébert and Martinet who doped lyotropic LCs with a water-based ferrofluid and observed that the magnetic field required to align LCs is reduced by a factor of thousand.[10]

Moreover, these materials provide striking magneto-optical properties due to the combination of the anisotropic optical properties of LCs and the large magnetic susceptibility of the magnetic particles. Many experiments have investigated the effects of an external magnetic field on the host LC matrix.[11–20] In particular, in a recent combined experimental and numerical study, it has been shown that the presence of magnetic particles, combined with an external magnetic field, can induce a nematic phase in an isotropic LC phase.[21]

Institut für Theoretische Physik, Technische Universität Berlin, Hardenberg Str. 36, 10623 Berlin, Germany. E-mail: shrivastav@tu-berlin.de, klapp@physik.tu-berlin.de

From a theoretical point of view, a standard model for spherical ferromagnetic particles is the so-called dipolar soft spheres (DSS), that is, spheres interacting *via* a steep isotropic repulsion and anisotropic forces stemming from embedded point dipoles. The equilibrium structure of DSS in a LC matrix composed of Gay–Berne ellipsoids is well studied theoretically[22–24] and *via* computer simulations for different sizes of the two species.[25–27] In particular, Monte Carlo (MC) simulations reveal that in the absence of an external magnetic field the DSS form chains along the director of the nematic LC matrix. Furthermore, as the diameter of DSS is increased, the uniaxial spontaneous ordering changes to a biaxial lamellar phase.[26]

In order to control and improve the flow properties of such hybrid systems,[28] it is important to develop a better understanding of the equilibrium dynamics of different species, in particular, the translational mobility. In recent molecular dynamics (MD) simulations,[27] it has been observed that the DSS show normal diffusion if their sizes are much smaller than the suspending LC fluid. Nonetheless, the dynamics may become more complex when the two components have comparable sizes. In fact, the smaller size of the DSS leads to stark differences in the equilibrium self-assembly and also in the translational dynamics of the DSS.[27] The equilibrium self-assembly of a mixture with much smaller DSS particles is characterized by a significant fraction of rings of DSS appearing together with the chains. Here, we consider a situation where the size of the DSS is comparable to the width of the LCs. Then, the available free volume around the DSS is smaller and, therefore, the ring formation is less feasible.

Our main focus is on the dynamics of the DSS, and we note that, in the absence of a LC matrix, dilute dipolar fluids display a subdiffusive behavior at intermediate times due to the formation

of chains with head-to-tail ordering of the dipole moments.[29] This subdiffusive regime increases as the strength of dipolar coupling is increased. Also, at a dipolar coupling strength at which dipolar particles start to form chains, the translational diffusion coefficient shows a sudden decrease.[30] Thus, the chain-forming tendency of dipolar particles plays an important role in their dynamics. We would therefore expect that the situation gets even more complex in a hybrid system of DSS in a LC host. Here, the LC matrix provides a dense anisotropic environment which, as we will show, renders the dynamics of magnetic particles anomalous. This finding is indeed consistent with the behavior of a wide range of complex systems where a dense environment or a complex geometry leads to a subdiffusive motion of particles.[31–34]

In this work, we present a MD simulation study on the translational dynamics of a mixture of LC and DSS, where the sizes of both the species are comparable. We observe that the dynamics of DSS is indeed highly influenced by the LC matrix. At low densities at which the LC matrix is in an isotropic phase, the mean square displacement (MSD) of DSS shows a subdiffusive regime at intermediate times. The length of the subdiffusive regime grows as the strength of dipolar coupling is increased. Eventually it spans the entire simulation time window at high values of the dipolar coupling. The effect of the LC matrix on the dynamics of the DSS is particularly visible at high densities, where the LC matrix undergoes an I–N transition and enforces, in turn, an aligned state of the DSS.[26] The DSS then show diffusive behavior parallel to the nematic director but remain subdiffusive in the perpendicular direction.

The rest of the paper is organized as follows. In Section 2 we give the details of the model and simulation method. We present our results in Section 3. The equilibrium phase diagram of the mixture is discussed in Section 3.1. Using MSD (Section 3.2) and velocity autocorrelation functions (VACF) (Section 3.3), we demonstrate that the DSS show anomalous translational diffusion at low temperatures while the LC matrix shows a normal diffusive behavior at all densities and temperatures. Finally, in Section 4, we conclude the paper with a summary.

2 Simulation details

We consider a binary mixture of LC and DSS with a composition ratio of 80 : 20 and perform MD simulations in the *NVT* ensemble using the LAMMPS package.[35,36] The LCs are modeled by ellipsoids which are characterized *via* a (diagonal) shape matrix $\boldsymbol{S} = \mathrm{diag}(\sigma_a,\sigma_b,\sigma_c)$ and a (diagonal) energy matrix $\boldsymbol{E} = \mathrm{diag}(\varepsilon_a,\varepsilon_b,\varepsilon_c)$, where $\sigma_{a,b,c}$ are the lengths and $\varepsilon_{a,b,c}$ are the relative well depths of interaction along the three semiaxes of an ellipsoid. We note that the model investigated here slightly differs from that considered in Peroukidis *et al.*[27] as the mixing parameters are different.

The LCs interact *via* a generalized Gay–Berne (GB) potential which is defined as[36–38] (following the notations of Brown *et al.*[36])

$$U(\boldsymbol{A}_i,\boldsymbol{A}_j,\boldsymbol{r}_{ij}) = U_{\mathrm{r}}(\boldsymbol{A}_i,\boldsymbol{A}_j,\boldsymbol{r}_{ij})\eta_{ij}(\boldsymbol{A}_i,\boldsymbol{A}_j)\chi_{ij}(\boldsymbol{A}_i,\boldsymbol{A}_j,\hat{\boldsymbol{r}}_{ij}). \quad (1)$$

Here $\boldsymbol{A}_i$ is the rotation matrix for a particle i, used for the transformation from the lab frame to the body frame of reference. Furthermore, $\boldsymbol{r}_{ij}$ is the center-to-center distance vector between particles i and j, and $\hat{\boldsymbol{r}}_{ij}$ is the unit vector along $\boldsymbol{r}_{ij}$.

The function $U_{\mathrm{r}}(\boldsymbol{A}_i,\boldsymbol{A}_j,\boldsymbol{r}_{ij})$, which controls the distance dependence of the GB potential, is defined as

$$U_{\mathrm{r}}(\boldsymbol{A}_i,\boldsymbol{A}_j,\boldsymbol{r}_{ij}) = 4\varepsilon_0\left[\left(\frac{\sigma_0}{h_{ij}+\gamma\sigma_0}\right)^{12} - \left(\frac{\sigma_0}{h_{ij}+\gamma\sigma_0}\right)^{6}\right], \quad (2)$$

where ε_0 and σ_0 set the units of energy and length, γ is the shift parameter and $h_{ij} = r_{ij} - \left[\frac{1}{2}\hat{r}_{ij}^T\boldsymbol{G}_{ij}\hat{r}_{ij}\right]^{-1/2}$ is the distance of the closest approach between particles i, j with $\boldsymbol{G}_{ij} = \boldsymbol{A}_i^T\boldsymbol{S}_i^2\boldsymbol{A}_i + \boldsymbol{A}_i^T\boldsymbol{S}_j^2\boldsymbol{A}_j$. The second and third terms in eqn (1) are given by

$$\eta_{ij}(\boldsymbol{A}_i,\boldsymbol{A}_j) = \left[\frac{2s_is_j}{\det\left[\boldsymbol{G}_{ij}(\boldsymbol{A}_i,\boldsymbol{A}_j)\right]}\right]^{\nu/2}, \quad (3)$$

$$\chi_{ij}(\boldsymbol{A}_i,\boldsymbol{A}_j,\hat{\boldsymbol{r}}_{ij}) = [2\hat{\boldsymbol{r}}_{ij}^T\boldsymbol{B}_{ij}^{-1}(\boldsymbol{A}_i,\boldsymbol{A}_j)\hat{\boldsymbol{r}}_{ij}]^{\mu'}. \quad (4)$$

In eqn (3), $s_{i,j} = [\sigma_{a_{i,j}}\sigma_{b_{i,j}} + \sigma_{c_{i,j}}\sigma_{c_{i,j}}][\sigma_{a_{i,j}}\sigma_{b_{i,j}}]^{1/2}$ and $\boldsymbol{B}_{ij} = \boldsymbol{A}_i^T\boldsymbol{E}_i^2\boldsymbol{A}_i + \boldsymbol{A}_j^T\boldsymbol{E}_j^2\boldsymbol{A}_j$ with $\boldsymbol{S}_{i,j}$ and $\boldsymbol{E}_{i,j}$ representing the shape and energy matrices for particles i and j.

We consider uniaxial LCs with an aspect ratio of 3, *i.e.*, $\sigma_a^{\mathrm{e}} = \sigma_b^{\mathrm{e}} = \sigma_0$ and $\sigma_{\mathrm{c}}^{\mathrm{e}} = 3\sigma_0$. The relative energy well depth for side-to-side interaction is $\varepsilon_a^{\mathrm{e}} = \varepsilon_b^{\mathrm{e}} = \varepsilon_0$ and for end-to-end interaction is $\varepsilon_c^{\mathrm{e}} = 0.2\varepsilon_0$. For ellipsoids, these values of the energy parameters yield the energy of the side-to-side configuration five times stronger than that of the end-to-end configuration. The cut-off radius is set to $r_c^{\mathrm{GB}} = 4.0\sigma_0$ and the empirical parameters of GB potential are set to $\mu' = 1.0$, $\nu = 2.0$ and $\gamma = 1.0$. The parameter μ' is the same as μ used for GB in Brown *et al.*[36] Here, we have changed the notation, as in our case, μ is reserved for the dipole moment of the DSS.

The interaction among the LC and DSS is also modeled by a GB potential with shape and energy parameters for DSS taken as $\sigma_a^s = \sigma_b{}^s = \sigma_c{}^s = \sigma_0$ and $\varepsilon_a^s = \varepsilon_b{}^s = \varepsilon_c{}^s = \varepsilon_0$. The cutoff radius is taken the same as $r_{\mathrm{c}}^{\mathrm{GB}}$.

The DSS interact *via* a combination of a soft sphere potential and dipolar interactions.[39,40] The full potential for two DSS particles i and j with dipole moments $\boldsymbol{\mu}_i$ and $\boldsymbol{\mu}_j$ is defined as[40]

$$U(ij) = U_{\mathrm{SR}}(r_{ij}) + \frac{\boldsymbol{\mu}_i\cdot\boldsymbol{\mu}_j}{r_{ij}{}^3} - 3\frac{(\boldsymbol{\mu}_i\cdot\boldsymbol{r}_{ij})(\boldsymbol{\mu}_j\cdot\boldsymbol{r}_{ij})}{r_{ij}{}^5}, \quad (5)$$

where $U_{\mathrm{SR}}(r_{ij})$ is the shifted-force soft sphere interaction given as

$$U_{\mathrm{SR}}(r_{ij}) = U_{\mathrm{SS}}(r_{ij}) - U_{\mathrm{SS}}(r_c^{\mathrm{SS}}) - (r_c^{\mathrm{SS}} - r_{ij})\left.\frac{\mathrm{d}U_{\mathrm{SS}}}{\mathrm{d}r}\right|_{r=r_c^{\mathrm{SS}}}. \quad (6)$$

In eqn (6), the cutoff radius for soft sphere potential is set to $r_c^{\mathrm{SS}} = 2.5\sigma_0$, and

$$U_{\mathrm{SS}}(r_{ij}) = 4\varepsilon_0(\sigma_0/r_{ij})^{12}. \quad (7)$$

The long range dipolar interactions are treated with the three dimensional Ewald sum.[41,42]

The parameters that characterize the structure and phase behavior of the mixture are the reduced temperature $T^* = k_BT/\varepsilon_0$, the reduced number density $\rho^* = N\sigma_0^3/V$ (where N and V are the total number of particles and the total volume respectively), and the reduced dipole moment $\mu^* = \mu^2/\varepsilon_0\sigma^3$. Newton's equations of motion for force and torque are integrated in the *NVT* ensemble using the velocity Verlet algorithm. A reduced MD time step $\Delta t^* = \Delta t \Big/ \sqrt{m\sigma_0^2/\varepsilon_0} = 0.002$ is chosen and simulations are performed at fixed $\mu^* = 3.0$, various ρ^* and T^*. The value of T^* ranges from 2.0 to 0.6, *i.e.*, the range of dipolar coupling parameter $\lambda = \mu^2/k_BT\sigma_0^3$ is 4.5 to 15.0. We have set $\mu^* = 3.0$, therefore, a change in T^* is equivalent to a change in λ. We will use λ for DSS and the corresponding T^* for LCs while discussing our results.

Our simulated system consists of 3200 LC (N_e) and 800 DSS particles (N_s). We start with a mixture equilibrated at low density and high temperature and then quench it to desired T^*. Subsequently, we slowly compress the mixture keeping T^* constant by applying the Langevin thermostat.[43] At each compression step, the mixture is equilibrated for 4×10^6 time steps. For MSD calculations at different ρ^*, we performed additional production runs in the *NVT* ensemble for 10^7 time steps after equilibration. We took 100 time origins for averaging.

The self-diffusion constant D is obtained from the long-time behavior of MSD. For VACF calculations, short production runs up to 25 000 time steps are performed using temperature rescaling at a frequency of 1000 time steps. It should be noted that performing long production runs in the *NVE* ensemble is quite difficult for the mixture. Also, the Langevin thermostat affects the equilibrium fluctuations by applying random forces on the particles. Therefore, we use temperature rescaling during the VACF production runs in order to maintain the temperature. The timescale for temperature rescaling is chosen such that the VACF decays almost to zero in that time.

3 Results

In this section we first present our numerical results for the equilibrium phase diagram of the LC–DSS mixture at the selected dipole moment $\mu^* = 3.0$. Second, we discuss the translational dynamics of the two components. In particular, we investigate the respective MSDs and normalized VACF.

3.1 Equilibrium phase diagram

First, we identify the I–N transition by calculating the nematic order parameter S for the LC–DSS mixture. This order parameter is defined as the largest eigenvalue of the ordering tensor $\boldsymbol{Q}$. The components of the $\boldsymbol{Q}$-tensor are given by $Q_{\alpha\beta} = (1/N)\sum_{i=1}^{N}(1/2)\left(3\hat{\boldsymbol{u}}_\alpha^i\hat{\boldsymbol{u}}_\beta^i - \delta_{\alpha\beta}\right)$. Here, $\alpha, \beta = x,y,z$ and $\hat{\boldsymbol{u}}^i$ is, for LC, the orientation vector and for DSS, the unit dipole vector $\hat{\boldsymbol{\mu}}^i$. The nematic order parameters S_e and S_s for individual components, LC and DSS, are calculated separately using the respective $\boldsymbol{Q}$ tensor. The eigenvectors corresponding to S_e and S_s define the directors $\hat{\boldsymbol{n}}_e$ and $\hat{\boldsymbol{n}}_s$ for LC and DSS respectively.

In Fig. 1, we plot S_e for the LC matrix (shown by the color axis) as a function of ρ^* and T^*. At low ρ^* and high T^*, the LC matrix remains in an isotropic phase while it undergoes an I–N transition at high ρ^* and low T^* values. The DSS chains follow the LC matrix and undergo an I–N transition at the same values of ρ^* and T^* (not shown here but visible in the snapshots in Fig. 2). The dashed lines in the plot represent the contours of different S_e values. We consider the line corresponding to $S_e = 0.4$ as an approximate I–N transition line obtained *via* MD simulations. We note here that, although the I–N phase transition is well understood for pure LCs and also for mixtures of LCs and DSS, it is difficult to obtain the precise location of the transition line *via* MD simulations. This is due to the possible inadequacy of the MD simulations to access the available phase space. One should, indeed, use sophisticated multicanonical Monte Carlo schemes such as histogram reweighting and successive umbrella sampling in order to sample the phase space uniformly.

For the illustration of the actual structure, the snapshots of the mixture corresponding to two state points (marked in red squares) are plotted in Fig. 2. At $\rho^* = 0.36$ and $T^* = 1.4$, the mixture is in an isotropic phase. As shown in Fig. 2(a), the LCs and the DSS chains (shown in Fig. 2(c)) are randomly oriented. Furthermore, Fig. 2(b) and (d) show that at $\rho^* = 0.36$ and $T^* = 0.8$, the LC matrix and DSS chains are both in a nematic phase. Also, the two nematic directors $\hat{\boldsymbol{n}}_e$ and $\hat{\boldsymbol{n}}_s$ are aligned almost parallel to each other which is consistent with the previous MC simulations.[25,26]

3.2 Mean-square displacements

We, next, analyze the translational dynamics of the two components of the mixture using MSD which is defined as

$$\langle \Delta r^2(t) \rangle = \frac{1}{N_{e,s}} \sum_{i=1}^{N_{e,s}} \left\langle |\boldsymbol{r}_i(t+t_0) - \boldsymbol{r}_i(t_0)|^2 \right\rangle, \qquad (8)$$

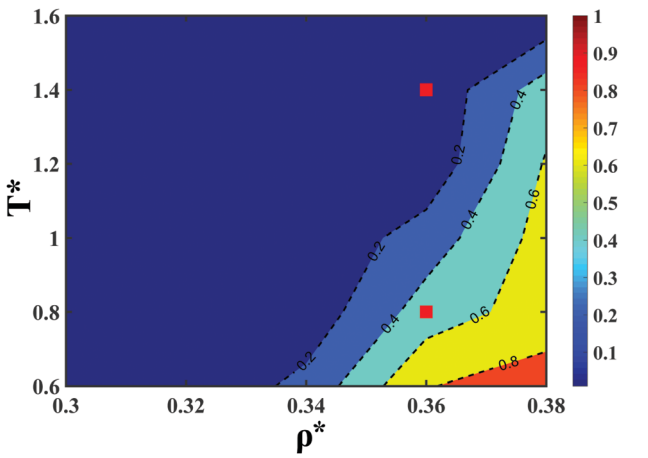

Fig. 1 The ρ^*–T^* phase diagram of the LC matrix. The color axis shows the nematic order parameter S_e, and dashed lines mark the contours of different S_e values. The dashed line corresponding to $S_e = 0.4$ is considered as the I–N phase transition line obtained *via* MD simulations. Red squares represent state points (0.36, 1.4) and (0.36, 0.8) in the isotropic and nematic phases, respectively. Snapshots corresponding to these two state points are shown in Fig. 2.

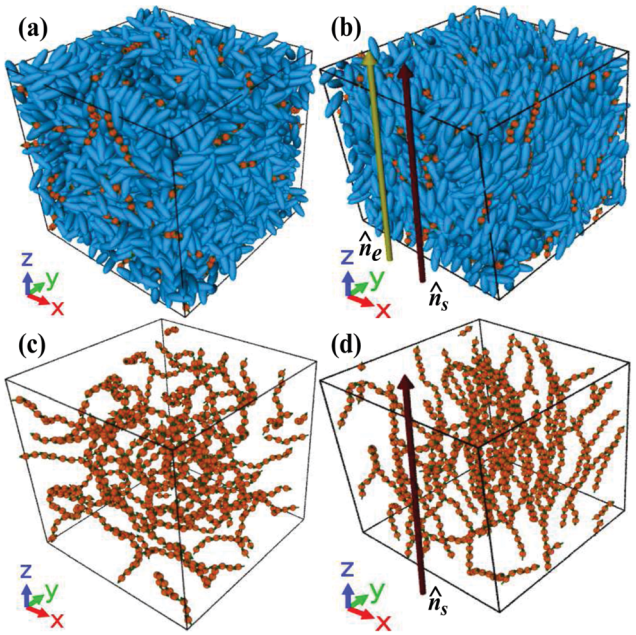

Fig. 2 Snapshots of the LC–DSS mixture at the state points marked by the red squares in Fig. 1. (a) Snapshot of the LC–DSS mixture at $\rho^* = 0.36$ and $T^* = 1.4$, (b) snapshot of the LC–DSS mixture at $\rho^* = 0.36$ and $T^* = 0.8$. (c) and (d) The DSS chains in the absence of the LC matrix for the state points considered in (a) and (b), respectively. All the snapshots are prepared using software OVITO.[44]

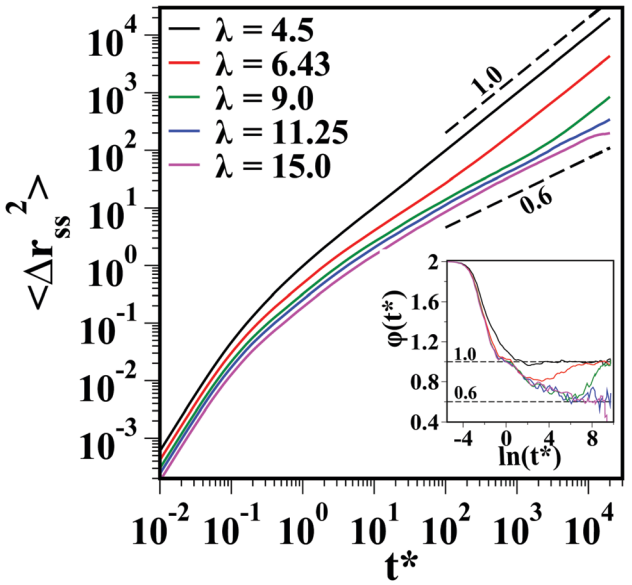

Fig. 3 MSD of DSS in the isotropic regime for $\rho^* = 0.3$ at $\lambda = 4.5$, 6.43, 11.25, and 15.0. At low λ, the MSD has a slope of 1.0 at large t (shown by a black dashed line). At large λ, subdiffusive behavior is observed with an exponent of 0.6. The inset shows the instantaneous slope ϕ of MSDs, which saturates to 1.0 for low λ while to 0.6 for large λ at long times.

where $\boldsymbol{r}_i(t)$ is the position of the particle at time t, t_0 is the time origin for MSD calculations, and angular bracket corresponds to the averaging over the total number of particles of a species, time origins and number of samples. To extract the longtime behavior of MSD, we calculate the instantaneous slopes, $\phi(t)$, of the MSD curves which is defined as

$$\phi(t) = \mathrm{d}\{\ln(\langle \Delta r^2(t)\rangle)\}/\mathrm{d}\{\ln(t)\}. \quad (9)$$

The slope of MSD curves at long times is given by

$$\alpha = \lim_{t\to\infty} \phi(t). \quad (10)$$

Diffusive behavior in the MSD is characterized by $\alpha = 1$ while subdiffusive and superdiffusive behaviors in the MSD correspond to $\alpha < 1$ and $\alpha > 1$ respectively.

In the nematic phase, the displacements of particles are resolved in the components parallel, $\Delta\boldsymbol{r}_{||}$, and perpendicular, $\Delta\boldsymbol{r}_{\perp}$, to the LC/DSS nematic director $\hat{\boldsymbol{n}}_{\mathrm{e,s}}$ at t_0 and the corresponding MSDs ($\langle \Delta r_{||}{}^2\rangle$ and $\langle \Delta r_{\perp}{}^2\rangle$) are calculated.[45,46] For LCs we can extract diffusion coefficients using the Stokes–Einstein relation, which in three dimensions reads $D = (1/6t)\lim_{t\to\infty}\langle \Delta r^2(t)\rangle$. The diffusion constants in the directions parallel and perpendicular to the nematic director are defined as

$$D_{||,\perp} = (1/2t)\lim_{t\to\infty}\langle \Delta r_{||,\perp}{}^2(t)\rangle. \quad (11)$$

3.2.1 Diffusional behavior of the dipolar particles. The MSDs of the DSS in the isotropic phase are plotted in Fig. 3 for $\rho^* = 0.3$ and various values of λ. For all $\lambda < 11.25$, the MSDs show three different regimes, ballistic at short times, subdiffusive at intermediate times and diffusive at long times. At low λ, the subdiffusive regime is rather short, however, as λ is increased the subdiffusive regime grows, and for $\lambda > 9.0$ at $\rho^* = 0.3$, it spans the entire simulation time window. The crossover from diffusion to subdiffusion at long times with increasing λ is more evident in the inset of Fig. 3. Here $\phi(t^*)$ is plotted for different MSD curves (shown in Fig. 3) as a function of t^* at $\rho^* = 0.3$. Clearly, at low λ, $\phi(t^*)$ saturates to 1 while it saturates to 0.6 at higher λ at long times. A region with a slope less than 1 exists at all $\lambda > 4.5$ which grows with increasing λ and eventually extends over the entire simulation time window.

In order to understand the longtime behavior of the MSD of the DSS at different ρ^* and λ, we have obtained a state diagram of α as a function of ρ^* and λ, see Fig. 4. Here, the color axis represents α and a black solid line shows the I–N transition, which appears at high ρ^* and λ. For $\lambda < 7.0$, α remains close to 1.0 for all considered ρ^*, reflecting normal diffusive behavior of MSDs. As λ is increased, the longtime behavior becomes subdiffusive at high densities and for $\lambda > 11.0$, the dynamics of DSS appears to be subdiffusive even at lower densities.

For a better understanding of the crossover of the longtime behavior of MSDs, we explore α along the two black dashed lines shown in Fig. 4. The vertical dashed line represents fixed ρ^* (= 0.3) and different λ, while the horizontal dashed line corresponds to fixed λ (= 11.25) and different ρ^*s.

The variation of α as a function of λ at a fixed $\rho^* = 0.3$ (along the vertical dashed line in Fig. 4) is shown in Fig. 5(a). Clearly, α shows a crossover from 1.0 to 0.6 as λ is increased. A similar crossover (Fig. 5(b)) is observed when ρ^* is varied at fixed $\lambda = 11.25$. However, Fig. 4 suggests that λ has to be large (>7.0) in order to see a crossover as a function of ρ^*.

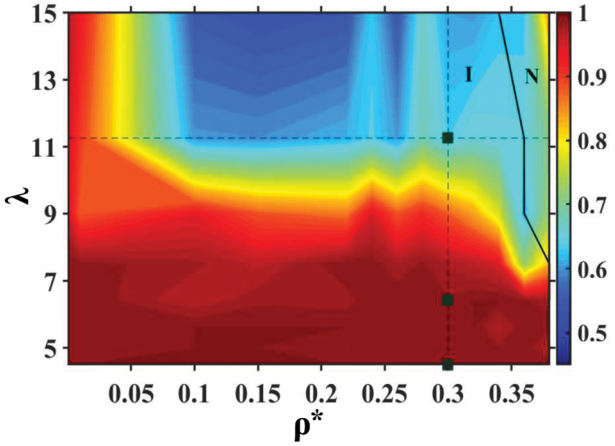

Fig. 4 Contour map showing α (see eqn (10)), extracted from the long-time MSD of DSS, as a function of λ (corresponding T^* can be obtained using $T^* = 9.0/\lambda$) and ρ^*. One observes a subdiffusive regime at large λ in the isotropic phase. The black solid line represents the I–N transition. The vertical and horizontal dashed lines correspond to fixed ρ^* (= 0.3) and fixed λ (= 11.25), respectively. The green squares, marked on the ρ = 0.3 (vertical) line, show three state points λ = 4.5, 6.43 and λ = 11.25 at ρ^* = 0.3.

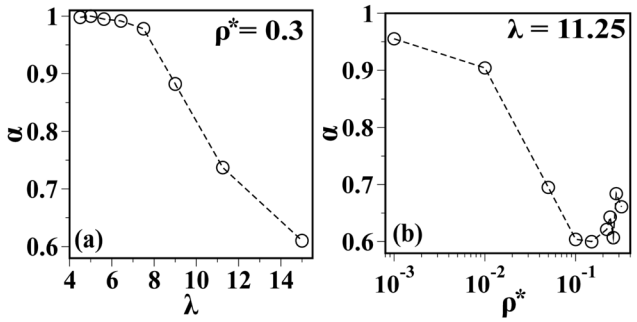

Fig. 5 Longtime slopes, α, of MSDs of DSS, (a) data for ρ^* = 0.3 as a function of λ and (b) data for λ = 11.25 as a function of ρ^*.

In the case of pure DSS, at ρ^* = 0.05 and λ = 7.0 and in the absence of an external magnetic field, a sublinear regime in the MSDs is observed at intermediate times which later turns into a diffusive behavior.[29] Also, for pure DSS, the self-diffusion constant decreases as λ is increased. A sudden drop in the diffusion constant at a critical λ is observed which is due to the chain formation of DSS.[30] In both of these studies[29,30] on the pure dipolar fluids, the range of λ is limited to 1–7.0 where the longtime behavior is always diffusive. For the present LC–DSS mixture in the isotropic phase, we observe a monotonic decrease of the self-diffusion constant D^* of the DSS as functions of both λ and ρ^*, provided that the longtime behavior of the MSD of the DSS is diffusive. This is illustrated in Fig. 6(a) and (b) respectively.

We also note that for pure dipolar soft core dumbbells,[47] one observes a crossover from longtime diffusive to subdiffusive dynamics at very high dipolar couplings which can be attributed to the network formation. In the present case (the LC–DSS mixture), the subdiffusion at large λ can also be attributed to the chain forming tendency of DSS. As shown in Fig. 7(a), at low λ (*i.e.* at high T^*), the DSS chains are very small. As λ is increased

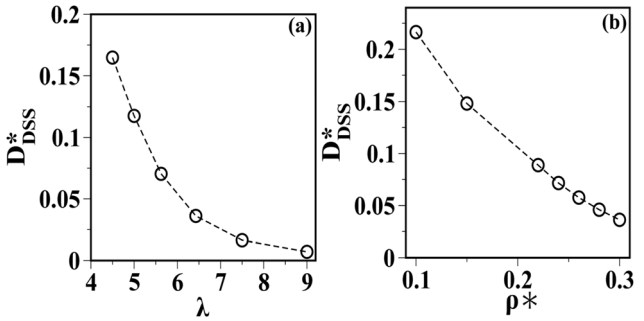

Fig. 6 Self-diffusion constants, D^*, of the DSS, (a) data for ρ^* = 0.3 as a function of λ and (b) data for λ = 6.43 as a function of ρ^*.

(Fig. 7(b) and (c)) the size of the DSS chains increases due to the strong coupling among the DSS. For a long isotropically distributed DSS chain, its collective motion in a dense environment (provided by the LC matrix) is difficult and, consequently, the DSS show an anomalous transport.

In the nematic phase, we fix λ = 11.25 (*i.e.* T^* = 0.8) and investigate the MSD for different ρ^* in the direction parallel and perpendicular to $\hat{\boldsymbol{n}}_s$. The reason behind such a choice of λ is that at this value, the DSS remain subdiffusive during the entire simulation time window and we expect the nematic ordering in the LC matrix to alter the DSS dynamics parallel to $\hat{\boldsymbol{n}}_s$. Fig. 8(a) shows $\langle \Delta r_{||}{}^2 \rangle$ of DSS, which has initial subdiffusive increase (reminiscent of the isotropic phase) which crosses over to a normal diffusive behavior at long times for all considered densities. The $\langle \Delta r_{\perp}{}^2 \rangle$ for DSS, plotted in Fig. 8(b), remains subdiffusive even at long times. The exponent of subdiffusion is $\sim$0.5 which is slower than the observed exponent in the isotropic regime for the total MSD at the same ρ^* and λ. The inset in Fig. 8(b) shows the trapping of DSS chains in the transient cylindrical cavities formed by the LC matrix in the nematic phase. This leads to the slowing down of the translational dynamics of the DSS in the direction perpendicular to the nematic director.

A possible mathematical model explaining the subdiffusion of the DSS in the isotropic phase of the LC–DSS mixture would be fractional Brownian motion.[32,33] However, the situation becomes complex in the nematic phase where an anisotropic environment provided by the LC matrix imposes a normal diffusion at long times in the direction parallel to the nematic director, while in the perpendicular direction the DSS become even slower. Taken together, for the present LC–DSS mixture, a suitable mathematical model is still lacking.

3.2.2 Diffusional behavior of the LC matrix. In contrast to the DSS, the LC matrix shows normal diffusive dynamics at all densities in the isotropic phase. In Fig. 9(a), we plot the MSDs of the LC matrix at fixed ρ^* and for various T^* (along the vertical dashed line in Fig. 4). Furthermore, Fig. 9(b) shows the MSDs of the LC matrix at fixed T^* (= 0.8) and for different ρ^* (along the horizontal dashed line in Fig. 4). In both of these cases, the longtime behavior of MSDs is normal diffusive for all ρ^* and T^*. Also, the diffusion constant decreases monotonically in both the cases, as can be seen in the insets of Fig. 9(a) and (b).

For the nematic phase, the $\langle \Delta r_{||}{}^2 \rangle$ of the LC matrix is plotted in Fig. 10(a). One observes a normal diffusion at long times for

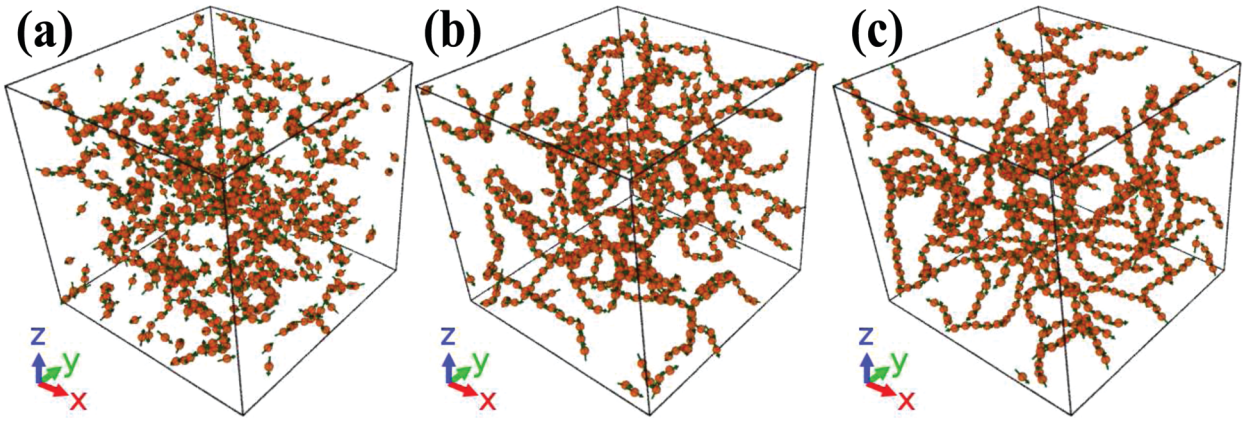

Fig. 7 (a). Snapshots showing DSS chains in the absence of the LC matrix at (a) λ = 4.5, (b) λ = 6.43, (c) and λ = 11.25 for ρ^* = 0.3 (see the green square points marked in the Fig. 4). At these values of λ and ρ^*, the mixture always remains in the isotropic phase, however, the length of the DSS chains increases as λ is increased.

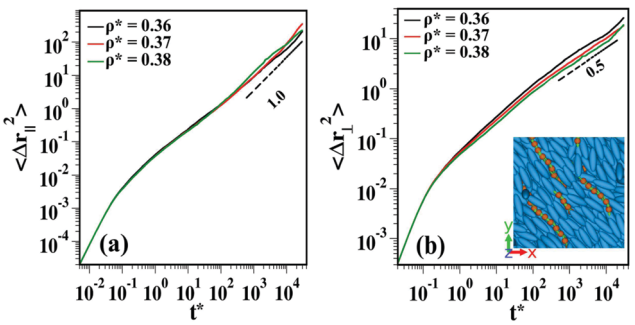

Fig. 8 (a). The component of the MSD of the DSS parallel to $\hat{\boldsymbol{n}}_s$ at ρ^* = 0.36, 0.37, 0.38 and λ = 11.25. The black dashed lines show a slope of 1.0. (b) The component of MSD perpendicular to $\hat{\boldsymbol{n}}_s$ for DSS at the same values of ρ^* and λ as in (a). The inset shows a top view of the snapshot for ρ^* = 0.37 and λ = 11.25. The MSD shows a subdiffusive behavior with an exponent of 0.5.

all ρ^* in the nematic regime. The inset in Fig. 10(a) shows the self-diffusion constants $D_{||}$ of the LC matrix parallel to $\hat{\boldsymbol{n}}_e$, which are extracted from the long time behavior of the $\langle \Delta r_{||}{}^2 \rangle$. We find that $D_{||}$ shows a non-monotonic behavior with increasing ρ^*, consistent with earlier studies of pure LCs.[46,48] Initially, at the onset of the I–N transition, LCs tend to align parallel to each other as this is the entropically favored state.[45,46] This results in the enhanced diffusion of the LCs parallel to the nematic director. However, at high densities (higher than the coexistence density) when the nematic phase is established, the diffusion of LCs slows down due to an increase of collisions with other LCs.

Fig. 10(b) shows the $\langle \Delta r_\perp{}^2 \rangle$ for the LC matrix. The long time behavior of $\langle \Delta r_\perp{}^2 \rangle$ is also normal diffusive. The $D_\perp{}^*$, extracted from $\langle \Delta r_\perp{}^2 \rangle$, plotted in the inset of Fig. 10(b), decreases monotonically with increasing ρ^* which is consistent with the earlier observations.[46,48]

3.3 Velocity autocorrelation functions

To explore the local environment of particles, we study the normalized VACF which is defined as $C_v(t) = \langle \boldsymbol{v}(t_0)\cdot\boldsymbol{v}(t + t_0)\rangle / \langle \boldsymbol{v}(t_0)\cdot\boldsymbol{v}(t_0)\rangle$.[43] The VACF resolved in the direction parallel and perpendicular to $\hat{\boldsymbol{n}}_s$, $C_{v_{||,\perp}}(t)$, is defined similar to $C_v(t)$, where only the respective components of the velocity are considered.

The results for the VACF for the DSS in the isotropic regime are plotted in Fig. 11(a) for λ = 4.5, 6.43 and 11.25 at ρ^* = 0.3 (along the vertical dashed line in Fig. 4). At low λ, the VACF decay smoothly without any oscillations. This indicates that the particles move essentially as unbounded objects, that is, chains are not yet formed. As λ is increased oscillations in the VACF are observed at short time scales which we attribute to chain formation. The oscillatory behavior at short times appears due to the rattling of DSS particles in the chain and indicates its "caging" due to strong dipolar coupling.

In the case of pure dipolar fluids in the isotropic phase at comparable λ,[49] such an oscillatory behavior is not observed (*cf.* the red curve in Fig. 11(a)). Also, for pure dipolar dumbbells, the oscillatory behavior in VACF is observed only at a very large λ where dipolar particles form a percolating network.[47] In our case, we observe the oscillatory behavior at $\lambda \sim 6.43$ where a percolating network is not yet expected (see, *e.g.*, Fig. 7(b), where long but not system spanning chains are visible at λ = 6.43). We understand the difference between the present mixed system and the pure system as follows: for pure dipolar fluids at λ = 6.66 in the isotropic phase,[49] the dipolar chains are randomly distributed and their collective motion is not hindered. Therefore, an oscillatory behavior does not occur in the VACF of the DSS. In the present system, the DSS chains experience a dense environment provided by the LC matrix, which is reflected in the form of oscillations in the VACF of the DSS.

It should also be noted that in Fig. 11(a) at small λ, where DSS chains are much shorter (*e.g.*, Fig. 7(a)), no negative lobe is present in the VACF, which suggests that the short DSS chains or single DSS particles do not feel the dense environment. As the size of the chain grows upon an increase of λ (for a fixed ρ^*), the role of the LC matrix becomes more evident in modifying the dynamics. Fig. 11(b) shows the VACF of DSS at a fixed T^* = 0.8 and various ρ^* (along the horizontal black dashed line in Fig. 4). Here, the oscillatory behavior can be seen at all considered ρ^*.

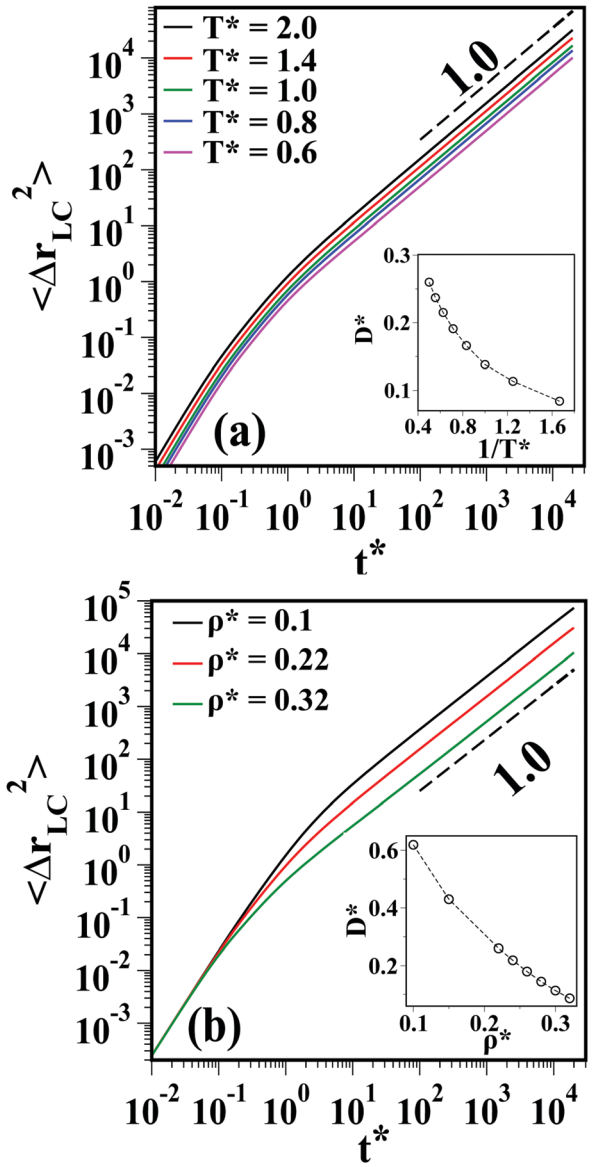

Fig. 9 (a) The MSD of the LC matrix in the isotropic phase. (a) The MSD of the LC matrix at fixed $\rho^* = 0.3$ (along the vertical black dashed line in Fig. 4) for $T^* = 2.0$, 1.4, 1.0, 0.8, and 0.6. The black dashed line shows a slope of 1.0. (b) The MSD of the LC matrix at a fixed $T^* = 0.8$ (along the horizontal black dashed line in Fig. 4) and $\rho^* = 0.1$, 0.22 and 0.32. The inset in both the figures shows the variation of self-diffusion constant as a function of $1/T^*$ and ρ^* respectively.

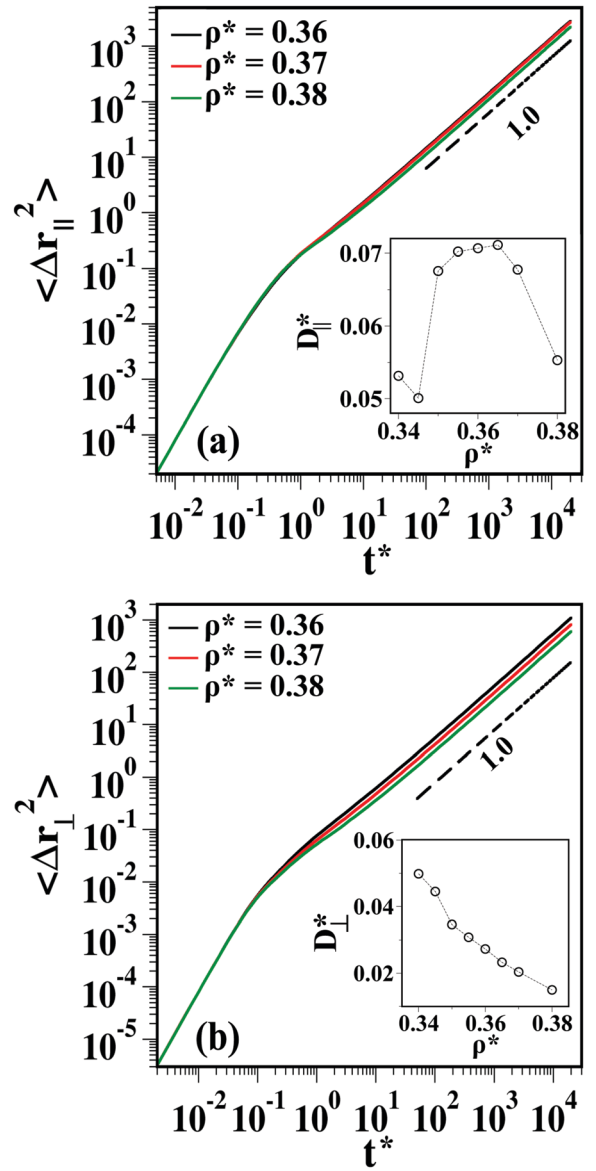

Fig. 10 The MSD of the LC matrix in the nematic phase. (a) The component of MSD parallel to $\hat{\boldsymbol{n}}_e$ for $\rho^* = 0.36$, 0.37 and 0.38 at $T^* = 0.8$. (b) The component of MSD perpendicular to $\hat{\boldsymbol{n}}_e$ for the same ρ^* and T^* as in (a). The longtime behavior of MSDs in all the three cases is diffusive as shown by the black dashed line with a slope of 1.0. The insets in (a) and (b) show the variation of $D_{\parallel}^*$ and $D_{\perp}^*$ with ρ^*.

In the nematic phase, $C_{v_{\parallel}}(t)$ for the DSS chains, plotted in Fig. 11(c) (shown by a red dashed line) decays faster than $C_{v_{\perp}}(t)$ (represented by a green dot–dashed line). The oscillations after the smooth initial decay are present in both the components. This is contrary to earlier observations for pure DSS where oscillations in $C_{v_{\perp}}$ are not found.[49] The oscillations in the parallel component arise due to the strong dipolar interactions which force the particles to remain in the chain. In the present case, the oscillations in the perpendicular component are the result of the confinement of the DSS chains in a narrow cylindrical channel formed by the LC matrix as shown in the inset of Fig. 11(c). Such an oscillatory behavior is peculiar to the dipolar fluids confined in a narrow space.[50]

We now turn to the VACF for the LC matrix. The results for the isotropic phase along the two dashed lines shown in Fig. 4 are plotted in Fig. 12. Similar to the earlier observations, Fig. 12(a) shows that the VACF do not show any negative lobe for the whole range of T^* considered in the isotropic phase at $\rho^* = 0.3$ (along the vertical black dashed line in Fig. 4). At lower T^*, a plateau appears which later converts into a minimum and a maximum.[46] A similar behavior is observed (Fig. 12(b)) at fixed $T^* = 0.8$ and various ρ^* (along the horizontal black dashed line in Fig. 4).

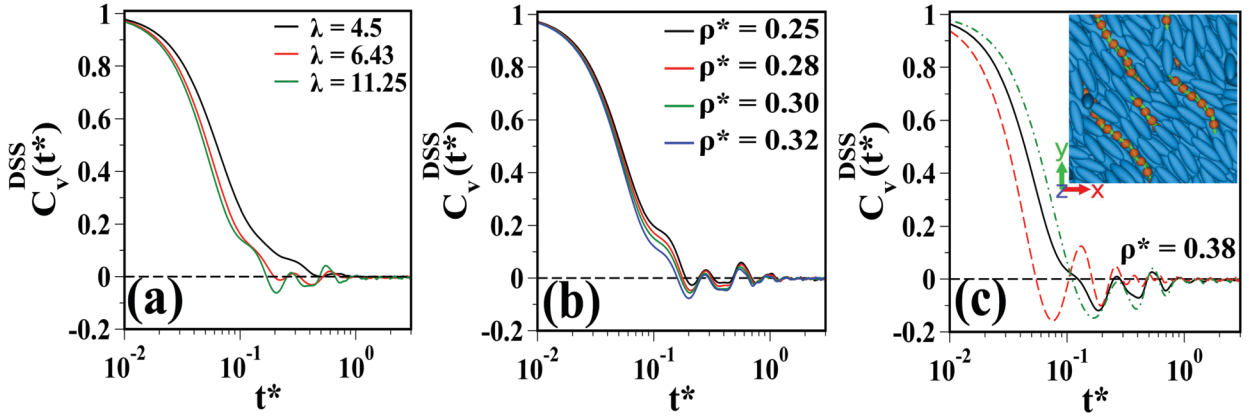

Fig. 11 The VACF of the DSS in the isotropic phase (a) for λ = 4.5, 6.43, and 11.25 at a fixed ρ^* = 0.3 (along the vertical black dashed line in Fig. 4) and (b) for ρ^* = 0.25, 0.28, 0.3, and 0.32 at λ = 11.25 (along the horizontal black dashed line in Fig. 4). (c) The VACF for DSS in the nematic regime at ρ^* = 0.38 and λ = 11.25. The red dashed and green dot–dashed lines represent the functions $C_{v_\parallel}(t)$ and $C_{v_\perp}(t)$. The inset shows a top view of the snapshot for ρ^* = 0.37 and λ = 11.25.

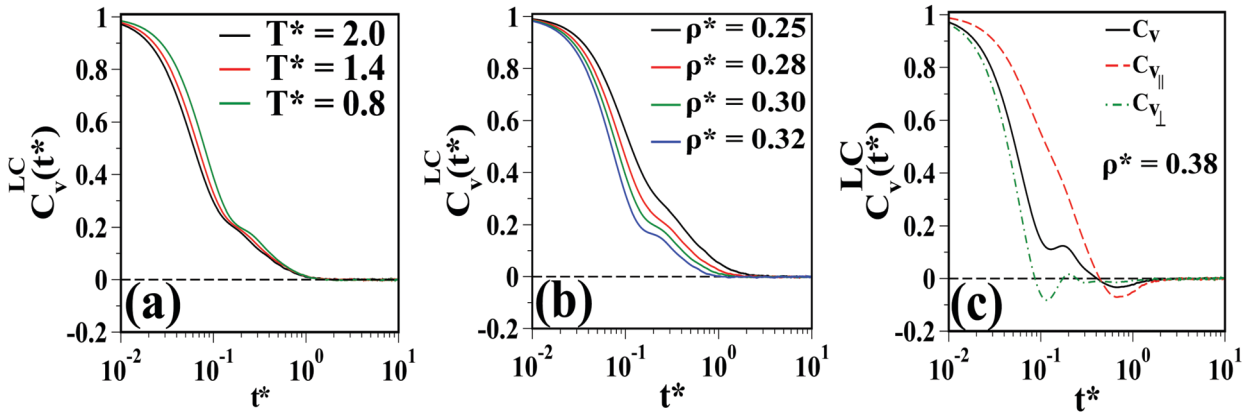

Fig. 12 The VACF of the LC matrix in the isotropic phase (a) for T^* = 2.0, 1.4, and 0.8 at fixed ρ^* = 0.3 (along the vertical black dashed line in Fig. 4) and (b) for ρ^* = 0.25, 0.28, 0.3, and 0.32 at T^* = 0.8 (along the horizontal black dashed line in Fig. 4). (c) The VACF for LC in the nematic regime at the ρ^* = 0.38 and T^* = 0.8. The red dashed and green dot–dashed lines represent $C_{v_\parallel}(t)$ and $C_{v_\perp}(t)$. The inset shows $C_{v_\parallel}(t)$ for ρ^* = 0.34, 0.35, 0.36, and 0.38.

Finally, the VACF of the LCs in the nematic regime for ρ^* = 0.38 and T^* = 0.8 is plotted in Fig. 12(c). The "shoulder" (the minimum and the subsequent maximum), which was observed at higher isotropic densities (*cf.* Fig. 12(b)), becomes more pronounced in the nematic regime. Furthermore, the decay of $C_{v_\parallel}(t)$ is slower than that of $C_{v_\perp}(t)$ consistent with the larger value of $D_{||}{}^*$. We observe a small negative region in $C_{v_\parallel}(t)$ which is an indicator of the high density of the mixture. As discussed in earlier studies,[46] the oscillatory behavior in $C_{v_\perp}(t)$ (shown by a green dot–dashed line in Fig. 12(c)) is due to the periodic rebounds of the LC particles in the direction perpendicular to $\hat{\boldsymbol{n}}_e$.

3.3.1 Signature of the subdiffusion in the VACF. So far we have analyzed the short-time behavior of the VACF of the DSS in order to investigate the local environment around the DSS. We, now, show that the subdiffusive behavior, observed in the MSD of the DSS, is also reflected in the VACF. To this end, we start with the Green–Kubo relation in three dimensions,[51]

$$D = \frac{1}{3}\int_0^\infty \langle \boldsymbol{v}(t') \cdot \boldsymbol{v}(0)\rangle \mathrm{d}t'. \tag{12}$$

Here, $t' = t - t_0$ is the time elapsed from the time origin taken at t_0. The VACF is related to the MSD as,[31,51]

$$\frac{1}{3}\langle \boldsymbol{v}(t) \cdot \boldsymbol{v}(0)\rangle = \frac{1}{6}\frac{\mathrm{d}^2}{\mathrm{d}t^2}\langle \Delta r^2(t)\rangle \tag{13}$$

Inserting eqn (13) into eqn (12) we obtain,

$$D = \frac{1}{3}\int_0^\infty \langle \boldsymbol{v}(t') \cdot \boldsymbol{v}(0)\rangle \mathrm{d}t' = \frac{1}{6}\frac{\mathrm{d}}{\mathrm{d}t'}\langle \Delta r^2(t')\rangle\Big|_{t'\to\infty}. \tag{14}$$

In simulations, we need to consider a "sufficiently large" time interval τ up to which numerical integration is performed in order to calculate the diffusion coefficient. Starting from this, we define a time (interval) dependent diffusion coefficient $D(\tau)$ by rewriting eqn (14) as,

$$D(\tau) = \frac{1}{3}\int_0^\tau \langle \boldsymbol{v}(t') \cdot \boldsymbol{v}(0)\rangle \mathrm{d}t' = \frac{1}{6}\frac{\mathrm{d}}{\mathrm{d}t'}\langle \Delta r^2(t')\rangle\Big|_{t'\to\tau}. \tag{15}$$

Therefore, for a diffusive process, in the limit of large τ, $D(\tau)$ saturates to the diffusion coefficient obtained *via* the Stokes–Einstein relation $\langle \Delta r^2(t') = 6Dt'\rangle$. Whereas, in the cases where the longtime behavior of the MSD is subdiffusive with an

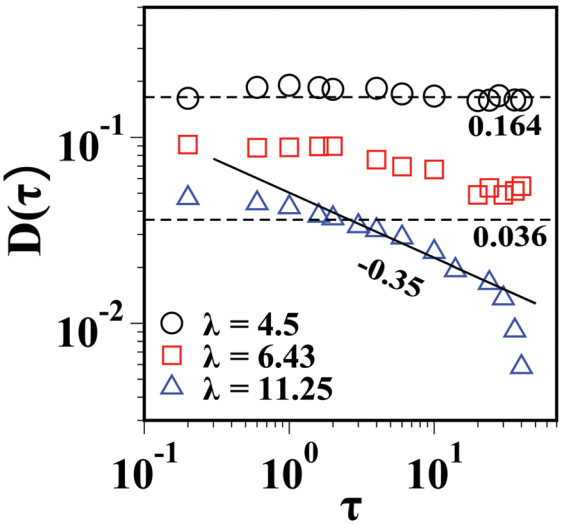

Fig. 13 Variation of the time dependent diffusion coefficient $D(\tau)$ calculated from the VACF of the DSS as a function of time interval τ for λ = 4.5, 6.43 and 11.25 at ρ^* = 0.3. The black dashed lines show the value of D obtained from the MSD of the DSS for λ = 4.5 and 6.43. The solid black line represents a slope of −0.35.

exponent α, $D(\tau)$ should show a power-law decay as a function of τ with an exponent $(\alpha - 1)$.

In Fig. 13, we plot $D(\tau)$ as a function of τ calculated from the VACF of the DSS for λ = 4.5, 6.43 and 11.25 at ρ^* = 0.3 (the green filled squares marked on the vertical dashed line in Fig. 4). Clearly, for λ = 4.5 and 6.43, $D(\tau)$ saturates to D which is calculated from the longtime behavior of the corresponding MSD of the DSS (values of D are shown by dashed black lines in Fig. 13). Furthermore, for λ = 11.25, $D(\tau)$ shows a power-law decay with an exponent of −0.35, which is consistent with the exponent of subdiffusion obtained from the corresponding longtime behavior of the MSD of the DSS. Thus, our numerical results confirm the relation between the VACF and the MSD in the longtime limit. The slight discrepancy in the saturated value of $D(\tau)$ for λ = 6.43 and the sudden drop in $D(\tau)$ for λ = 11.25 at long times may be due to the lack of statistical averaging.

4 Summary and outlook

To summarize, we have presented a detailed MD simulation study on the translational dynamics in a LC–DSS mixture, in which both the species have comparable sizes. Our main finding is that in such a mixture, the DSS show a crossover from normal to anomalous translational dynamics in the isotropoic regime as λ is increased. At small λ the DSS chain lengths are shorter and, therefore, they can easily diffuse inside the LC matrix. However, as λ is increased, the lengths of the DSS chains increase and eventually their translational dynamics become subdiffusive. In this sense, the orientationally disordered LC matrix provides a complex environment which strongly influences the diffusion of host particles.

In the nematic regime, the LC particles, due to their cooperative movement and reorientation in the direction parallel to $\hat{\boldsymbol{n}}_e$, form a cylindrical channel and force the DSS chains to align along the channel. As a consequence, the DSS diffuse normally parallel to $\hat{\boldsymbol{n}}_e$ while remain subdiffusive in the perpendicular direction. The anisotropic translational dynamics of DSS in narrow slit pores is well studied, and enhanced diffusion of DSS parallel to the channel has been observed.[50] The DSS chains in the present case show similar behavior.

The strong confinement imposed by the LC matrix is also reflected in the VACF of the DSS, which show an oscillatory behavior not only in the isotropic regime but also in the nematic regime. The VACF of the LC matrix show a minimum and maximum at short times in the isotropic regime. In the nematic regime, only the perpendicular component of the VACF of the LC matrix shows an oscillatory behavior while the parallel component decays smoothly at high nematic densities.

In this work, we have demonstrated that the LC matrix strongly modifies the translational dynamics of the DSS whereas the LC dynamics remains essentially unaffected. A further study of the rotational dynamics of such mixtures is necessary in order to develop a better understanding of the intrinsic timescles. Also, it will be interesting to explore the effect of an external magnetic field on the dynamics of different components of the mixture, as it has been experimentally shown that a weak magnetic field affects the ordering in these systems.[21]

We believe that the present study will be very helpful in understanding the rheology of ferronematics as the interplay of intrinsic and shear induced timescales gives rise to intriguing behavior in these complex fluids. Work in these directions is underway.

Conflicts of interest

The authors have no conflict of interest.

Acknowledgements

We gratefully acknowledge funding support from the Deutsche Forschungsgemainschaft (DFG) *via* the priority program SPP 1681. GPS would like to thank Jürgen Horbach, Nima H. Siboni and Sascha Gerloff for fruitful discussions.

Notes and references

1 *Liquid Crystals with Nano and Microparticles*, ed. J. P. F. Lagerwall and G. Scalia, World Scientific, 2016, vol. 1 and 2.
2 J. P. F. Lagerwall and G. Scalia, *Curr. Appl. Phys.*, 2012, **12**, 1387.
3 H. K. Bisoyi and S. Kumar, *Chem. Soc. Rev.*, 2011, **40**, 306.
4 C. Blanc, D. Coursault and E. Lacaze, *Liq. Cryst. Rev.*, 2013, **1**, 83.
5 P. de Gennes and F. Brochard, *J. Phys.*, 1970, **31**, 691.
6 C. P. Lapointe, T. G. Mason and I. I. Smalyukh, *Science*, 2009, **326**, 1083.
7 C. Scherer and A. M. F. Neto, *Braz. J. Phys.*, 2015, **35**, 718.
8 Q. Liu, P. J. Ackerman, T. C. Lubensky and I. I. Smalyukh, *Proc. Natl. Acad. Sci. U. S. A.*, 2016, **113**, 10479.
9 J. Rault, P. E. Cladis and J. P. Burger, *Phys. Lett. A*, 1970, **32**, 199.

10 L. Liebert and A. Martinet, *J. Phys., Lett.*, 1979, **40**, L-363.
11 A. M. F. Neto and M. M. F. Saba, *Phys. Rev. A: At., Mol., Opt. Phys.*, 1986, **34**, 3483.
12 S.-H. Chen and N. M. Amer, *Phys. Rev. Lett.*, 1983, **51**, 2298.
13 P. Kopčanský, N. Tomašovičová, M. Koneracká, V. Závišová, M. Timko, A. Džarová, A. Šprincová, N. Éber, K. Fodor-Csorba, T. Tóth-Katona, A. Vajda and J. Jadzyn, *Phys. Rev. E: Stat., Nonlinear, Soft Matter Phys.*, 2008, **78**, 011702.
14 V. Berejnov, J.-C. Bacri, V. Cabuil, R. Perzynski and Y. Raikher, *Europhys. Lett.*, 1998, **41**, 507.
15 N. Podoliak, O. Buchnev, O. Buluy, G. D'Alessandro, M. Kaczmarek, Y. Reznikov and T. Sluckin, *Soft Matter*, 2011, **7**, 4742.
16 O. Buluy, S. Nepijko, V. Reshetnyak, E. Ouskova, V. Zadorozhnii, A. Leonhardt, M. Ritschel, G. Schönhense and Y. Reznikov, *Soft Matter*, 2011, **7**, 644.
17 S. Kredentser, O. Buluy, P. Davidson, I. Dozov, S. Malynych, V. Reshetnyak, K. Slyusarenko and Y. Reznikov, *Soft Matter*, 2013, **9**, 5061.
18 A. Mertelj, D. Lisjak, M. Drofenik and M. Čopič, *Nature*, 2013, **504**, 237.
19 F. Arantes and S. Odenbach, *J. Magn. Magn. Mater.*, 2015, **390**, 91.
20 S. H. Navarro, P. Tierno, J. I. Mullol and F. Sagués, *Soft Matter*, 2011, **7**, 5109.
21 K. May, A. Eremin, R. Stannarius, S. D. Peroukidis, S. H. L. Klapp and S. Klein, *Langmuir*, 2016, **32**, 5085.
22 S. I. Burylov and Y. L. Raikher, *Mol. Cryst. Liq. Cryst.*, 1995, **258**, 123.
23 A. B. Ryskin, H. Pleiner and H.-W. Müller, *Eur. Phys. J. E: Soft Matter Biol. Phys.*, 2003, **11**, 389.
24 E. Jarkova, H. Pleiner, H.-W. Müller and H. R. Brand, *J. Chem. Phys.*, 2003, **118**, 2422.
25 S. D. Peroukidis, K. Lichtner and S. H. L. Klapp, *Soft Matter*, 2015, **11**, 5999.
26 S. D. Peroukidis and S. H. L. Klapp, *Phys. Rev. E: Stat., Nonlinear, Soft Matter Phys.*, 2015, **92**, 010501(R).
27 S. D. Peroukidis and S. H. L. Klapp, *Soft Matter*, 2016, **12**, 6841.
28 S. Odenbach, *Magnetoviscous Effects in Ferrofluids*, Springer, Berlin, Heidelberg, 2003.
29 J. Jordanovic, J. Sebastian and S. H. L. Klapp, *Phys. Rev. Lett.*, 2011, **106**, 038301.
30 A. Shreekumari and P. Ilg, *Phys. Rev. E: Stat., Nonlinear, Soft Matter Phys.*, 2013, **88**, 042315.
31 F. Höfling and T. Franosch, *Rep. Prog. Phys.*, 2013, **76**, 046602.
32 E. Barkai, Y. Garini and R. Metzler, *Phys. Today*, 2012, **65**, 29.
33 Y. Meroz and I. M. Sokolov, *Phys. Rep.*, 2015, **573**, 1.
34 J. Horbach, S. K. Schnyder and N. H. Siboni, *Eur. Phys. J.: Spec. Top.*, 2017, **226**, 3113.
35 S. Plimpton, *J. Comput. Phys.*, 1995, **117**, 1.
36 W. M. Brown, M. K. Petersen, S. J. Plimpton and G. S. Grest, *J. Chem. Phys.*, 2009, **130**, 044901.
37 R. Berardi, A. Costantini, L. Muccioli, S. Orlandi and C. Zannoni, *J. Chem. Phys.*, 2007, **126**, 044905.
38 R. Everaers and M. R. Ejtehadi, *Phys. Rev. E: Stat., Nonlinear, Soft Matter Phys.*, 2003, **67**, 041710.
39 D. Wei and G. N. Patey, *Phys. Rev. Lett.*, 1992, **68**, 2043.
40 J. A. Morenao-Razo, E. DÍaz-Herrera and S. H. L. Klapp, *Mol. Phys.*, 2006, **104**, 2841.
41 M. Schoen and S. H. L. Klapp, *Reviews of Computational Chemistry*, John Wiley and Sons, New York, 2007, vol. 24.
42 Z. Wang, C. Holm and H. W. Müller, *Phys. Rev. E: Stat., Nonlinear, Soft Matter Phys.*, 2002, **66**, 021405.
43 M. Allen and D. Tildesley, *Computer Simulation of Liquids*, Oxford University Press, Oxford, UK, 2006.
44 A. Stukowski, *Modell. Simul. Mater. Sci. Eng.*, 2010, **18**, 015012.
45 H. Löwen, *Phys. Rev. E: Stat. Phys., Plasmas, Fluids, Relat. Interdiscip. Top.*, 1999, **59**, 1989.
46 E. de Miguel, L. F. Rull and K. E. Gubbins, *Phys. Rev. A: At., Mol., Opt. Phys.*, 1992, **45**, 3813.
47 R. Blaak, M. A. Miller and J. P. Hansen, *Europhys. Lett.*, 2007, **78**, 26002.
48 M. P. Allen, *Phys. Rev. Lett.*, 1990, **65**, 2881.
49 D. Wei and G. N. Patey, *Phys. Rev. E: Stat. Phys., Plasmas, Fluids, Relat. Interdiscip. Top.*, 1993, **47**, 2954.
50 V. A. Froltsov and S. H. L. Klapp, *J. Chem. Phys.*, 2006, **126**, 114703.
51 D. Frenkel and B. Smit, *Understanding Molecular Simulation*, Academic Press, 2nd edn, 2001.

